

Two-dimensional velocity of the magnetic structure observed on 11 July 2017 by the Magnetospheric Multiscale spacecraft

Richard E. Denton¹, Roy B. Torbert², Kevin J Genestreti³, Hiroshi Hasegawa⁴, Roberto Manuzzo⁵, Gerard Belmont⁶, Laurence Rezeau⁵, Francesco Califano⁷, Rumi Nakamura⁸, Jan Egedal⁹, Olivier Le Contel¹⁰, James L Burch³, Ivan Dors², Matthew R Argall², Christopher T. Russell¹¹, Robert J. Strangeway¹¹, and Barbara L. Giles¹²

¹Dartmouth College

²University of New Hampshire

³Southwest Research Institute

⁴Institute of Space and Astronautical Science, JAXA

⁵Laboratoire de Physique des Plasmas

⁶LPP

⁷University of Pisa

⁸Space Research Institute

⁹UW-Madison

¹⁰CNRS/Ecole Polytechnique/Sorbonne Université/Université Paris-Saclay/Obser. de Paris

¹¹University of California Los Angeles

¹²NASA Goddard Space Flight Center

November 21, 2022

Abstract

In order to determine particle velocities and electric field in the frame of the magnetic structure, one first needs to determine the velocity of the magnetic structure in the frame of the spacecraft observations. Here, we show how to determine a two dimensional magnetic structure velocity for the magnetic reconnection event observed in the magnetotail by the Magnetospheric Multiscale (MMS) spacecraft on 11 July 2017. We use two different multi-spacecraft methods, Spatio-Temporal Difference (STD) and the recently developed polynomial reconstruction method. Both of these methods use the magnetic field measurements, and the reconstruction technique also uses the current density measured by the particle instrument. We find rough agreement between the results of our methods and with other velocity determinations previously published. We also explain a number of features of STD and show that the polynomial reconstruction technique is only likely to be valid within a distance of two spacecraft spacings from the centroid of the MMS spacecraft. Both of these methods are susceptible to contamination by magnetometer calibration errors.

Two-dimensional velocity of the magnetic structure observed on 11 July 2017 by the Magnetospheric Multiscale spacecraft

Richard E. Denton¹, Roy B. Torbert², Kevin J. Genestreti³, Hiroshi Hasegawa⁴,
Roberto Manuzzo^{5,6}, Gerard Belmont⁵, Laurence Rezeau⁵, Francesco Califano⁶,
Rumi Nakamura⁷, Jan Egedal⁸, Olivier Le Contel⁵, James L. Burch⁹, Ivan Dors²,
Matthew R. Argall², Christopher T. Russell¹⁰, Robert J. Strangeway¹⁰, and
Barbara L. Giles¹¹

¹Department of Physics and Astronomy, Dartmouth College, Hanover, New Hampshire, USA

²Institute for the Study of Earth, Oceans, and Space, University of New Hampshire, Durham, New Hampshire, USA.

³Institute for the Study of Earth, Oceans, and Space, Southwest Research Institute, Durham, New Hampshire, USA.

⁴Institute of Space and Astronautical Science, JAXA, Sagamihara, Japan.

⁵LPP, CNRS, Ecole polytechnique, Sorbonne Université, Observatoire de Paris, Université Paris-Saclay, PSL Research
University, Paris, France.

⁶Department of Physics E. Fermi, Università di Pisa, Italia

⁷Space Research Institute, Austrian Academy of Sciences, Graz, Austria.

⁸Department of Physics, University of Wisconsin-Madison, Madison, Wisconsin, USA.

⁹Space Science and Engineering Division Southwest Research Institute, San Antonio, Texas, USA.

¹⁰Institute of Geophysics and Planetary Physics, University of California at Los Angeles, Los Angeles, California, USA.

¹¹NASA Goddard Space Flight Center, Greenbelt, MD, USA.

Key Points:

- We demonstrate use of Spatio-Temporal Difference (STD) and polynomial reconstruction to determine the 2-D velocity of a magnetic structure
- Velocities from STD and reconstruction roughly agree with each other and with estimates from other references for the 11 July 2017 event
- Polynomial reconstruction is only likely to be accurate within a distance of 2 spacecraft spacings from the centroid of the MMS spacecraft

Abstract

In order to determine particle velocities and electric field in the frame of the magnetic structure, one first needs to determine the velocity of the magnetic structure in the frame of the spacecraft observations. Here, we show how to determine a two dimensional magnetic structure velocity for the magnetic reconnection event observed in the magnetotail by the Magnetospheric Multiscale (MMS) spacecraft on 11 July 2017. We use two different multi-spacecraft methods, Spatio-Temporal Difference (STD) and the recently developed polynomial reconstruction method. Both of these methods use the magnetic field measurements, and the reconstruction technique also uses the current density measured by the particle instrument. We find rough agreement between the results of our methods and with other velocity determinations previously published. We also explain a number of features of STD and show that the polynomial reconstruction technique is only likely to be valid within a distance of two spacecraft spacings from the centroid of the MMS spacecraft. Both of these methods are susceptible to contamination by magnetometer calibration errors.

1 Introduction

In magnetic reconnection, plasma flows toward the magnetic X line (a magnetic null in the reconnection plane, in which it appears as an X point) with an inflow velocity and is accelerated and ejected in an orthogonal direction with an outflow velocity because of the large curvature of the magnetic field in the vicinity of the X line [e.g., *Vasyliunas, 1975; Sonnerup, 1979*]. To determine these velocities, one needs to determine the frame of reference in which the X line is stationary. Thus an important part of the process of understanding a magnetic reconnection event is to determine the velocity of the magnetic structure relative to the observing spacecraft. Although on large scales, plasma may be “frozen in” to the magnetic field, at least in directions perpendicular to the magnetic field, this is typically not the case on small scales close to the X line, especially in the region known as the electron diffusion region [*Hesse et al., 2011, 2014*].

Shi et al. [2019] has recently reviewed methods to determine a coordinate system and magnetic structure velocity. Methods to determine the velocity include calculating the deHoffmann-Teller frame in which the electric field is approximately zero, various types of timing analysis, various reconstruction methods, and the Spatial-Temporal Difference (STD) method [*Shi et al., 2006*]. STD has been recently used by *Denton et al. [2016a,b]* and *Yao et al. [2016, 2018]* to determine the time-dependent velocity of a magnetic structure in the normal direc-

59 tion. *Alm et al.* [2017] recently used STD to calculate the time-dependent two-dimensional
 60 velocity of the spacecraft moving through a structure of ion-scale magnetopause flux ropes.
 61 *Manuzzo et al.* [2019] recently described difficulties with calculating the structure velocity in
 62 multiple dimensions, and suggested new approaches to calculate the velocity. Their method
 63 includes the possibility of including mild time dependence. The implementation of STD that
 64 we will describe in this paper is somewhat simpler, and assumes that the structure velocity is
 65 constant on the timescale of motion across the spacecraft separation, as did the original STD.

66 Recently *Torbert et al.* [2018a, 2020] introduced a new method for reconstruction of
 67 the instantaneous magnetic field in the region close to the MMS spacecraft using a polyno-
 68 mial expansion of the magnetic field with input from the spacecraft measurements of the
 69 magnetic field and particle current density. *Denton et al.* [2020] described a number of vari-
 70 ations of Torbert et al.’s method and tested the validity of the magnetic field model during
 71 times in which the magnetic structure was roughly 2 dimensional. In this paper, we will use
 72 Denton et al.’s Reduced Quadratic model that results from the assumption that $\lambda_1 \gg \lambda_2 \gg$
 73 λ_3 , where λ_i are the eigenvalues of Minimum Directional Derivative (MDD) analysis that
 74 determines the eigenvectors of the gradient of the vector magnetic field [*Shi et al.*, 2005].

75 We will apply our implementation of STD to calculate the velocity of the magnetic
 76 structure for the magnetotail reconnection event on 11 July 2017 described by *Torbert et al.*
 77 [2018b]. In the process, we will elucidate several aspects of the method. Then we will use
 78 the new polynomial reconstruction method to get a second estimate of the velocity.

79 The paper is organized as follows. In section 2, we describe the data and methods to be
 80 used, in section 3 we calculate the velocity of the magnetic structure using the two methods,
 81 and in section 4 we discuss our results, including comparison to previous estimates of the
 82 structure velocity from other methods.

83 **2 Data and Methods**

84 **2.1 MMS Data**

85 In this paper we will examine the magnetotail reconnection event on 11 July 2017 at
 86 22:34 UT. The time t will be measured in seconds after this time. This event was first stud-
 87 ied by Torbert et al. [*Torbert et al.*, 2018b], and has been the subject of a number of other
 88 papers [e.g., *Genestreti et al.*, 2018; *Nakamura et al.*, 2019; *Hasegawa et al.*, 2019; *Egedal*
 89 *et al.*, 2019]. The position of the spacecraft was in the magnetotail at $[-21.53, 4.23, 3.64] R_E$

90 in geocentric solar ecliptic (GSE) coordinates. The average separation between spacecraft
 91 was 18.3 km. We will be concentrating on the interval $t = 1.6\text{--}2.8$ s, during which the mag-
 92 netic structure was moving tailward, so that, relative to that structure, the MMS spacecraft
 93 skimmed past the reconnection X line nearly along but below the current sheet.

94 As discussed by *Denton et al.* [2020], we use the magnetic field and particle current
 95 density from the MMS mission [*Burch et al.*, 2015]. The fluxgate magnetometer (FGM)
 96 [*Russell et al.*, 2016] and search coil magnetometer (SCM) [*Le Contel et al.*, 2016] data are
 97 combined into a single product with original resolution of 0.12 ms [*Fischer et al.*, 2016; *Ar-*
 98 *gall et al.*, 2018]. We boxcar average this to 1 ms resolution. We calculate the particle cur-
 99 rent density, \mathbf{J} , from the burst mode ion and electron bulk velocity moments from the Fast
 100 Plasma Instrument (FPI) [*Pollock et al.*, 2016], using the formula $\mathbf{J} = en'_e (\mathbf{V}_i - \mathbf{V}_e)$, where
 101 e is the proton charge, n'_e is an adjusted electron density, and \mathbf{V}_i and \mathbf{V}_e are respectively the
 102 ion and electron bulk velocity. Within the time interval 1.6 s to 3.1 s (a slightly more com-
 103 plete time interval than the one we will analyze), a factor f is found at each time step such
 104 that $fn_e (\mathbf{V}_i - \mathbf{V}_e)$ averaged over the spacecraft is closest in a least-squares sense to the cur-
 105 rent density from the “curlometer” [*Robert et al.*, 1998] technique, that determines the cur-
 106 rent density from $\nabla \times \mathbf{B}/\mu_0$ using the spacecraft \mathbf{B} values and spatial separations. During
 107 this time interval, the values of f varied between 0.65 and 1.13. The quantity n'_e is the me-
 108 dian value of f for the time series, 0.844, multiplied by the observed n_e . This adjustment was
 109 made because \mathbf{J}_{curl} is considered to be more accurate than \mathbf{J} ; but using the constant in time
 110 median value of f allowed for the possibility of real time variation of \mathbf{J} averaged over the
 111 spacecraft.

112 The resolution of the electron moments was 30 ms, and that of the ions (measured col-
 113 lectively) was 150 ms. These are interpolated to 1 ms resolution. Though we keep the data
 114 at this resolution, the effective time resolution is much less, since we here boxcar average the
 115 data to 0.5 s resolution. Despite this smoothing, use of the combined FGM/SCM magne-
 116 tometer product reduces noise relative to that found using the burst mode data, probably by
 117 reducing the error associated with interpolating the individual MMS spacecraft field values
 118 (with different timestamps) to common times.

119 Because of this averaging, our methods are likely to be accurate only in some average
 120 sense on a timescale ≤ 0.5 s. Our reconstruction technique has previously revealed some
 121 significant time dependence [*Denton et al.*, 2020], and we find time variation in the structure

122 velocity also here using both STD and the polynomial reconstruction (Figure 3a). There may
 123 very well be more detailed short timescale behavior that we do not describe.

124 2.2 Structure velocity from STD

125 The Spatio-Temporal Difference (STD) method of *Shi et al.* [2006] is based on the con-
 126 vection equation,

$$\frac{d\mathbf{B}}{dt} = \frac{\partial\mathbf{B}}{\partial t} + \mathbf{V}_{\text{sc}} \cdot \nabla\mathbf{B}, \quad (1)$$

127 where \mathbf{V}_{sc} is the velocity of the spacecraft relative to the magnetic structure and $d\mathbf{B}/dt$
 128 the rate of change of the magnetic field observed at the spacecraft. Shi et al. neglected the
 129 partial time derivative relative to the convective term to get

$$\frac{d\mathbf{B}}{dt} = -\mathbf{V}_{\text{str}} \cdot \nabla\mathbf{B}, \quad (2)$$

130 where $\mathbf{V}_{\text{str}} = -\mathbf{V}_{\text{sc}}$ is the structure velocity relative to the spacecraft. This equation can be
 131 solved as a set of simultaneous equations at the resolution of the magnetometer data, yielding
 132 time-dependent structure velocities.

133 Assume that an event L - M - N coordinate system has been established [*Denton et al.*,
 134 2018; *Genestreti et al.*, 2018, and references therein]. Usually we want L to be the direction
 135 of the reconnection magnetic field; N may be the normal direction across the current sheet,
 136 and M is the other direction. In the common two dimensional description of magnetic re-
 137 connection, M is assumed to be the direction of invariance, but sometimes the most invariant
 138 direction has a different orientation than that of M if the L direction is determined based on
 139 maximum variance of \mathbf{B} [*Denton et al.*, 2016a, 2018].

140 A local time-dependent coordinate system l - m - n is based on the eigenvectors of Mini-
 141 mum Directional Derivative (MDD) analysis [*Shi et al.*, 2005]. In MDD, a symmetric tensor
 142 is formed by multiplying the gradient of the vector magnetic field by its transpose, and then
 143 the eigenvectors of the resulting symmetric tensor are found. In this case, n is the maximum
 144 gradient direction, m is the minimum gradient direction, and l is the intermediate gradient di-
 145 rection. (The definitions of l and m are reversed from those recently used by *Manuzzo et al.*
 146 [2019].) If the coordinate system is time invariant, l - m - n would be the same as the event co-
 147 ordinate system L - M - N if the gradient is a minimum in the M direction.

As described by *Shi et al.* [2006], and further in Appendix A, we can solve (2) for the local gradient $k = l, m, \text{ or } n$ component of the structure velocity, $\mathcal{V}_{\text{str},k}$, using

$$\mathcal{V}_{\text{str},k} = -\mathcal{B}_{dt,i} \mathcal{G}_{k,i} / \lambda_k, \quad (3)$$

where $\mathcal{B}_{dt,i}$ is the i component of the time derivative of \mathbf{B} as observed by the spacecraft, $\mathbf{G} = \nabla \mathbf{B}$, λ_k is one of the MDD eigenvalues, the calligraphy letters indicate that the quantities are in the local gradient (l - m - n) coordinates system, and repeated indices are summed. Expanding this out explicitly,

$$\mathcal{V}_{\text{str},k} = -\frac{1}{\lambda_k} \left(\frac{d\mathcal{B}_n}{dt} \frac{\partial \mathcal{B}_n}{\partial X_k} + \frac{d\mathcal{B}_l}{dt} \frac{\partial \mathcal{B}_l}{\partial X_k} + \frac{d\mathcal{B}_m}{dt} \frac{\partial \mathcal{B}_m}{\partial X_k} \right), \quad (4)$$

where X is the position vector in the MDD eigenvector frame. From (4), we see that the dominant source of $\mathcal{V}_{\text{str},k}$ is from the term \mathcal{B}_i for which the product of its time derivative and spatial gradient in the X_k direction is the greatest.

For example, suppose that we can define a reconnection L - M - N coordinate system for which the largest variation is for B_L and the largest spatial variation is in the N direction [*Denton et al.*, 2018]. Then $\lambda_n \approx (\partial B_L / \partial X_N)^2$, and (4) would become

$$V_{\text{str},N} \approx -\frac{(dB_L/dt)(\partial B_L/\partial X_N)}{(\partial B_L/\partial X_N)^2} \sim -\frac{dX_N}{dt}. \quad (5)$$

(The minus sign is because the left-hand side of (5) is the structure velocity, but dX_N/dt on the right hand side of (5) is the time derivative of the spacecraft displacement relative to the structure.)

In the following text, we will drop the calligraphy notation, so, for instance, $V_{\text{str},n}$ is the structure velocity in the local MDDB n direction.

2.3 Reduced quadratic polynomial reconstruction model

As discussed by *Denton et al.* [2020], the 3D Reduced quadratic (RQ-3D) model was found by starting with the full quadratic expansion, and then reducing the number of terms based on the ordering $\partial/\partial n \gg \partial/\partial l \gg \partial/\partial m$. Because $\partial/\partial m$ is assumed to be small, we only allow “strictly linear” variation with respect to m . That is, the m -dependent terms are linear in m , and do not have l or n dependence. Then the m derivatives will be everywhere constant and therefore no greater than those determined from the linear gradients based on the MMS inter-spacecraft magnetic field variation. Because $\partial/\partial n$ is big, we also expect $\partial B_n/\partial n$ to be small because of $\nabla \cdot \mathbf{B} = 0$, so we also neglect $\partial^2 B_n/\partial n^2$ to ensure that $\partial B_n/\partial n$

174 remain small away from the spacecraft. This leads to neglect of other terms, as described in
 175 more detail by *Denton et al.* [2020]. The resulting model is

$$B_l = B_{l,0} + \frac{\partial B_l}{\partial n}n + \frac{\partial B_l}{\partial l}l + \frac{\partial B_l}{\partial m}m + \frac{\partial^2 B_l}{\partial n^2} \frac{n^2}{2} \quad (6)$$

$$B_m = B_{m,0} + \frac{\partial B_m}{\partial n}n + \frac{\partial B_m}{\partial l}l + \frac{\partial B_m}{\partial m}m + \frac{\partial^2 B_m}{\partial n^2} \frac{n^2}{2} + \frac{\partial^2 B_m}{\partial n \partial l}nl + \frac{\partial^2 B_m}{\partial l^2} \frac{l^2}{2} \quad (7)$$

$$B_n = B_{n,0} + \frac{\partial B_n}{\partial n}n + \frac{\partial B_n}{\partial l}l + \frac{\partial B_n}{\partial m}m + \frac{\partial^2 B_n}{\partial l^2} \frac{l^2}{2} \quad (8)$$

176 Neglecting the displacement current in the Ampere-Maxell law, $\mu_0 \mathbf{J}$ is the curl of (6–8),
 177 which is written out in Appendix B. (Here μ_0 is the permeability of free space.)

178 In addition to these equations, we have a constraint in order to ensure $\nabla \cdot \mathbf{B} = 0$. Taking
 179 the divergence of (6–8), we find

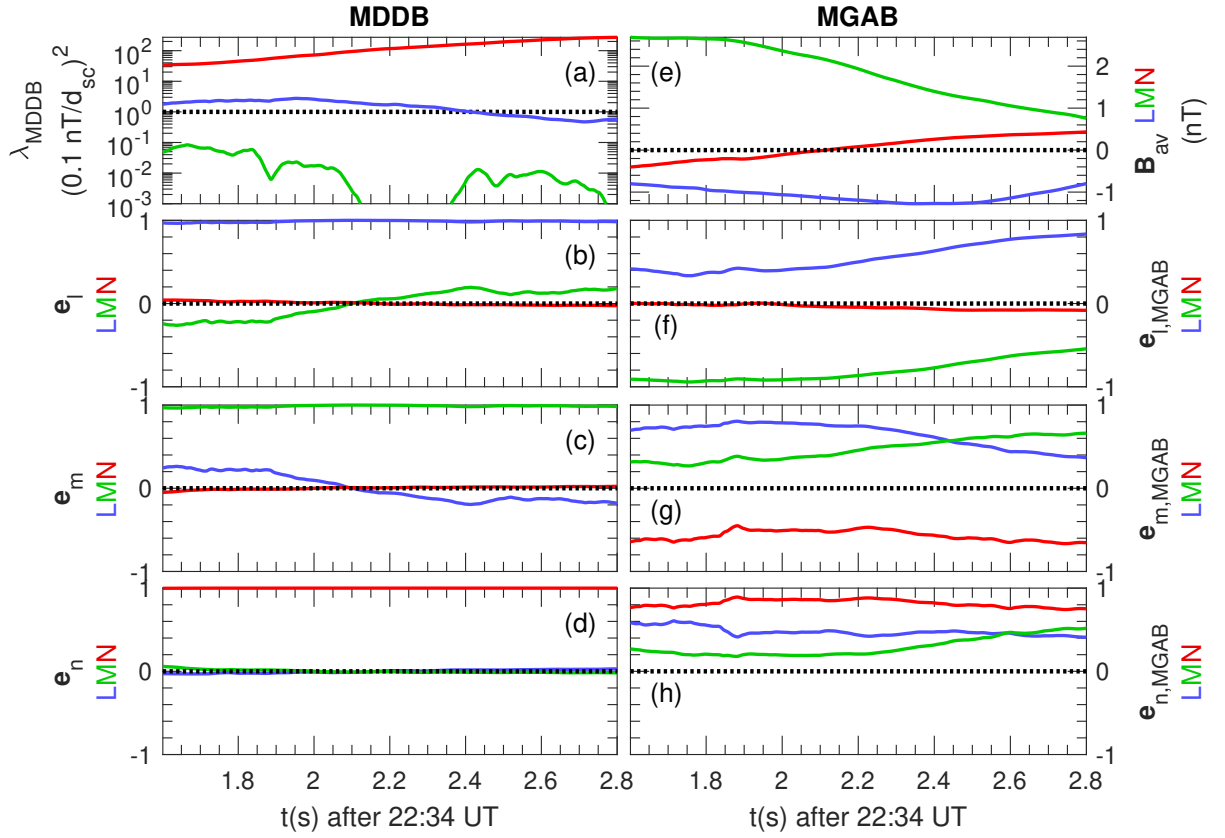
$$\frac{\partial B_n}{\partial n} + \frac{\partial B_l}{\partial l} + \frac{\partial B_m}{\partial m} = 0 \quad (9)$$

180 The three equations in (6–8) can be solved at each spacecraft location, leading to 12
 181 equations. Similarly the equations for $\mu_0 \mathbf{J}$ in Appendix B also yield 12 equations. With (9),
 182 there are a total of 25 equations that can be used to solve for 17 parameters for a best least-
 183 squares fit. A more detailed description of the method is given by *Denton et al.* [2020].

184 3 Results

185 3.1 MDD analysis

191 Figure 1 shows the results of Minimum Directional Derivative (MDD) and Minimum
 192 Gradient Analysis (MGA), both applied to the vector magnetic field [*Shi et al.*, 2019]. Fig-
 193 ure 1a shows the eigenvalues for MDDB, which are also the same as the eigenvalues for
 194 MGAB. (MGA will be described below.) Figure 1b–d shows the local (time-dependent)
 195 MDDB eigenvectors l , m , and n , respectively, expressed in terms of the global coordinates
 196 that we have chosen for this event, L - M - N . As one can see from Figure 1b–d, l , m , and
 197 n are approximately equal to L , M , and N , respectively. In fact, \mathbf{e}_N and \mathbf{e}_M were found by
 198 taking the mean components of \mathbf{e}_n and \mathbf{e}_m , making a slight adjustment of \mathbf{e}_M so that it was
 199 perpendicular to \mathbf{e}_N , and then getting \mathbf{e}_L from the cross product, $\mathbf{e}_M \times \mathbf{e}_N$. The local \mathbf{e}_n
 200 direction is found from the maximum gradient eigenvector, representing the direction of the
 201 maximum gradient across the current sheet. The local \mathbf{e}_m direction was the direction of the
 202 minimum gradient, so that an approximate two-dimensional representation of this system
 203 would include variation only in the N and L directions.



186 **Figure 1.** Minimum Directional Derivative (MDD) and Minimum Gradient Analysis (MGA). (a) MDDDB
 187 (or MGAB) eigenvalues; (b–d) local MDDDB l , m , and n eigenvectors, respectively, with blue, green, and
 188 red curves showing the L , M , and N components, where $[L;M;N] = [0.876,0.424,-0.230;-0.476,0.835,-$
 189 $0.275;0.075,0.351,0.936]$; (e) L - M - N components of the magnetic field averaged over the MMS spacecraft;
 190 (f–h) local MGAB eigenvectors in the same format as for MDDDB.

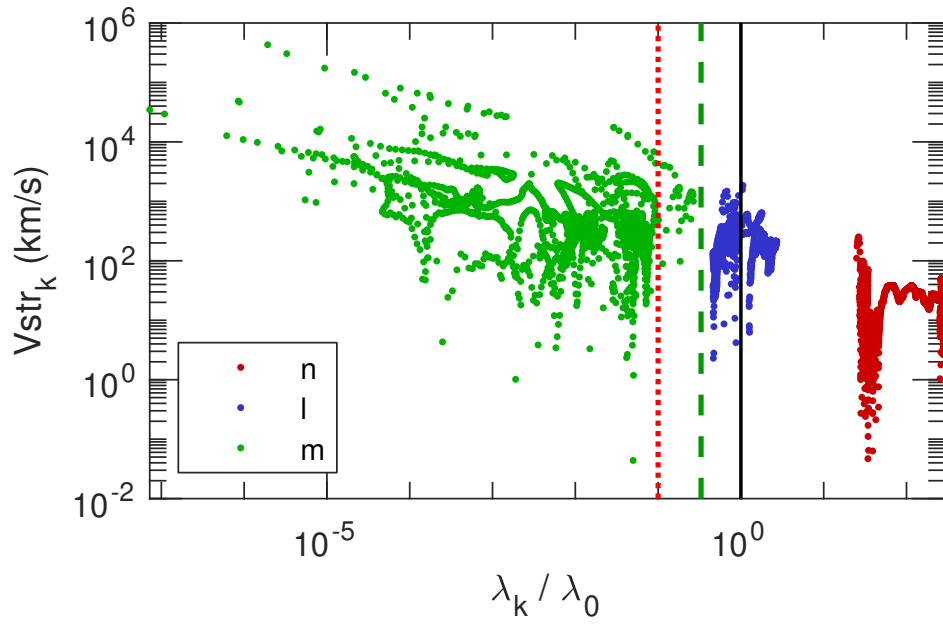
204 Note that the l and L directions might not well represent the Minimum Variance Anal-
 205 ysis (MVA) direction of maximum variance of the magnetic field [Sonnerup and Cahill,
 206 1967; Sonnerup and Scheible, 1998], which is often associated with L [e.g. Denton *et al.*,
 207 2018]. MGA is a local version of MVA [Shi *et al.*, 2019] that uses the magnetic gradient ma-
 208 trix at one particular time, as does MDD. But MGA compares the values of \mathbf{B} observed by
 209 the four spacecraft to find the components of \mathbf{B} that have the most or least variation. That
 210 is, while MDD finds the directions of largest and least gradient, MGA finds the directions
 211 of largest and least variance. In Figure 1f–1h, $\mathbf{e}_{l,\text{MGAB}}$, $\mathbf{e}_{m,\text{MGAB}}$, and $\mathbf{e}_{n,\text{MGAB}}$ are respec-
 212 tively the local MVA-like maximum, intermediate, and minimum variance directions. Fig-
 213 ure 1f shows that $\mathbf{e}_{l,\text{MGAB}}$ is at first mostly in the $-M$ direction (green curve with largest ab-
 214 solute value). Later in the interval, there is more variation in the L direction (blue curve with
 215 largest absolute value).

216 We will at first examine this event using the L - M - N coordinate system based on MDDB
 217 as described above, with $[L; M; N] = [0.879, 0.419, -0.230; -0.472, 0.837, -0.277; 0.077, 0.352, 0.933]$.
 218 These coordinate directions differ by 15° , 16° , and 7° , respectively, from the L , M , and N di-
 219 rections of Torbert *et al.* [2018b], and by 40° , 39° , and 11° , respectively, from the hybrid
 220 MDD-B/MVA- v_e L , M , and N directions of Genestreti *et al.* [2018] (coordinate system 14 in
 221 their Table A1).

222 3.2 Velocity from STD

223 Equation (4) shows that the k th component of the structure velocity in the local MDDB
 224 coordinates, $V_{\text{str},k}$ ($\mathcal{V}_{\text{str},k}$ in (4)), has the k th eigenvalue, λ_k , in the denominator. Thus very
 225 small values of λ_k can lead to very large values of the corresponding velocity component.
 226 In principle, if the structure were truly two-dimensional and time invariant, and λ_k became
 227 very small, the numerator of (4) would also become very small, so that the resulting veloc-
 228 ity would be well behaved. But in practice, non-two dimensionality, time dependence, and
 229 approximations and errors in the calculation of the gradients can result in small values of
 230 the denominator without correspondingly small values of the numerator. Thus very small λ_k
 231 yields what we call a “singularity”, leading to unrealistically large $V_{\text{str},m}$ [see discussion by
 232 Shi *et al.*, 2019; Manuzzo *et al.*, 2019].

233 Since the relative DC magnetometer calibration of the MMS spacecraft is rated to be
 234 accurate to 0.1 nT, values of λ_k below $\lambda_0 = (0.1 \text{ nT}/d_{\text{sc}})^2$, where d_{sc} is the average spacecraft



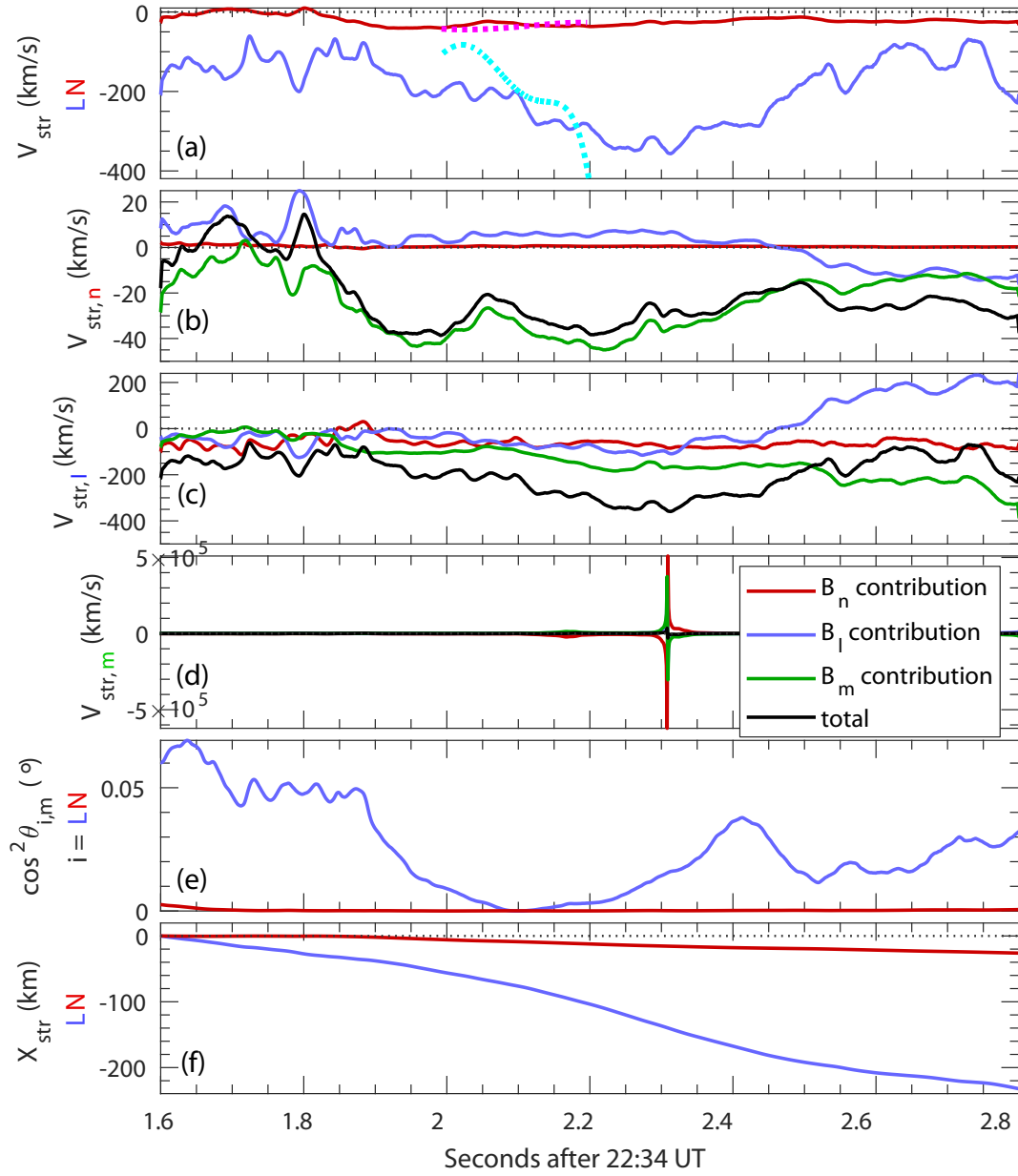
233 **Figure 2.** Velocity components in the local MDDB directions versus eigenvalue. The velocity components,
 234 $V_{\text{str},k}$, for the interval $t = 1.6$ s to 2.8 s are plotted versus the local normalized MDDB eigenvalue, λ_k/λ_0 ,
 235 for the maximum gradient n component (red dots), the intermediate gradient l component (blue dots), and
 236 the minimum gradient m component (green dots), where $\lambda_0 = (0.1 \text{ nT}/L_{sc})^2$. The vertical dashed green and
 237 dotted red lines are at values of λ_k/λ_0 equal to 0.33 and 0.1, respectively.

240 spacing (here, 18.3 km), could be suspect [Shi *et al.*, 2019]. Calibration errors are especially
 241 serious, because they can lead to systematic (constant) error in the gradients. Figure 2 shows
 242 components of the STD structure velocity, $V_{str,k}$, in the local MDDB eigenvector directions
 243 versus the normalized eigenvalue, λ_k/λ_0 . One evidence that the gradient in a direction is not
 244 being calculated accurately would be that the inferred structure velocity, $V_{str,k}$, increases as
 245 λ_k decreases. This is because, in principle, there should not be any correlation between the
 246 velocity in a certain direction and the gradient of the magnetic field in that same direction.

247 Evidence of this can be seen in Figure 2. Note that the velocities of the minimum gra-
 248 dient component of the structure, $V_{str,min}$ (green dots), increase with decreasing λ_k/λ_0 for
 249 $\lambda_k/\lambda_0 < 10^{-1}$, that is, for data points to the left of the red vertical dotted line in Figure 2.
 250 However, there is no indication that the velocities increase with respect to decreasing λ_k/λ_0
 251 for larger eigenvalues than about $\lambda_k/\lambda_0 = 0.25$. For the time being, we are going to proceed
 252 with the assumption that the velocities measured in the intermediate gradient direction (blue
 253 points in Figure 2) are accurate. This is equivalent to assuming that eigenvalues, λ_k/λ_0 , are
 254 accurately calculated if their values are greater than 0.33, that is, for data points to the right
 255 of the vertical green dashed line in Figure 2. Note also that our main attention will be for the
 256 velocity before about 2.2 s, for which λ_l/λ_0 is above unity (Figure 1a).

267 Figure 3 shows the results of the STD analysis. The solid curves in Figure 3a show the
 268 components of the 2D STD magnetic structure velocity formed by projection of the local n
 269 and l components onto the global N (red solid curve) and L (blue solid curve) directions.
 270 The black curves in Figures 3b—d are the n , l , and m components of the structure velocity,
 271 respectively. Comparison of the black curve in Figure 3b with the red curve in Figure 3a, and
 272 the black curve in Figure 3c with the blue curve in Figure 3a, shows that the n and l compo-
 273 nents of the STD velocity are nearly equal to the N and L components, respectively, as sug-
 274 gested by Figure 1d and 1b, respectively. The red, blue, and green curves in Figures 3b—d
 275 show the contributions to $V_{str,k}$ for $k = n, l$, or m from the B_n, B_l , and B_m dependent terms,
 276 respectively, in (4). As indicated by the very large values of $V_{str,m}$ in Figure 2, $V_{str,m}$ is of-
 277 ten grossly inaccurate if the MDDB eigenvalue is very small. Figure 3d, which shows a sin-
 278 gularity in $V_{str,m}$, is included only to remind the reader of this fact.

279 Figures 3b and 3c show some possibly unexpected results. If the spacecraft cross the
 280 entire current sheet, often the largest magnetic variation is in the B_L component, due to the
 281 strong dependence of B_L on N . Then one would expect the value of $V_{str,n}$ to be dominated



257 **Figure 3.** Spatial-Temporal Difference (STD) results. (a) STD velocity components in the L (blue solid
 258 curve) and N (red solid curve) directions calculated using only contributions from the MDDDB local n and l
 259 directions; (b–d) STD velocity component in the MDDDB local (b) n , (c) l , and (d) m directions, where the
 260 black curve is the total component $V_{str,k}$ for $k = n, l$, or m , and the red, blue, and green curves are the contri-
 261 butions to $V_{str,k}$ from the B_n , B_l , and B_m terms in (4), respectively; (e) squared cosine of the angle between
 262 the L (blue curve) or N (red curve) direction and the m direction; (f) net STD displacement from $t = 1.6$ s in
 263 the L (blue curve) and N (red curve) directions. The dotted curves in Figure 3a are the L (cyan curve) and N
 264 (magenta curve) velocity components found from RQ-3D reconstruction during the time when the centroid
 265 of the MMS spacecraft was within two average spacecraft separations, d_{sc} , from the X line of the magnetic
 266 structure.

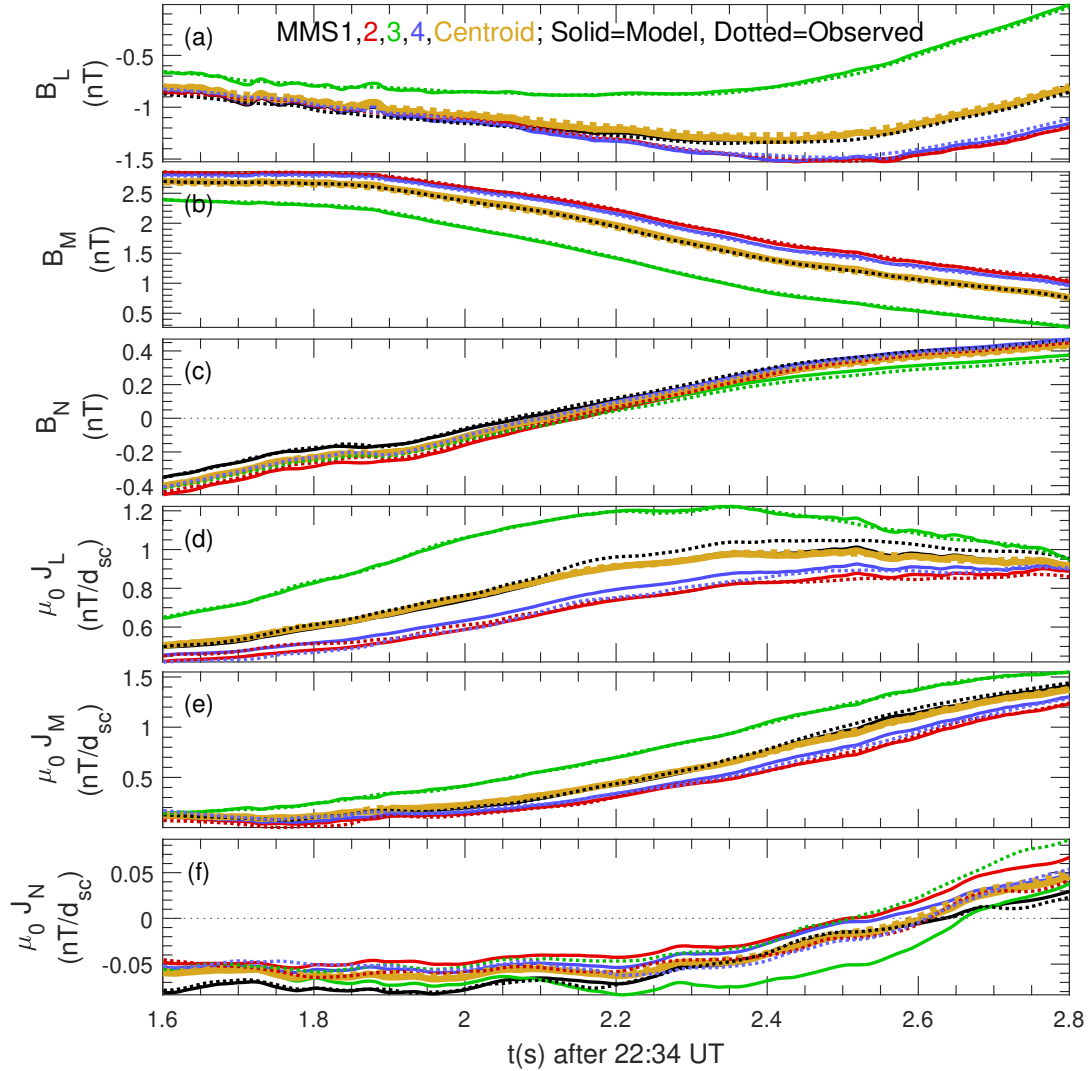
282 by the contribution from the B_L -dependent terms in (4), as was assumed in the derivation of
 283 (5). But Figure 3b shows that the value of $V_{str,n}$ is dominated by the contribution from the
 284 B_m -dependent terms in (4). This is because for this event the MMS spacecraft were skim-
 285 ming close to but under the current sheet [Torbert *et al.*, 2018b; Hasegawa *et al.*, 2019], so
 286 that there was little variation in B_L over the time plotted in Figure 3. From Figure 1e, we can
 287 see that B_m is larger in magnitude than B_l , and that the variation in B_m is also larger, except
 288 at the end of the time interval after about $t = 2.6$ s. Consequently, $V_{str,n}$ is dominated by the
 289 contributions from the B_m -dependent terms in (4) (green curve in Figures 3b) up until about
 290 $t = 2.6$ s, after which the B_l -dependent terms also contribute significantly (blue curve in
 291 Figures 3b).

292 Similarly, in the frame of reference of the magnetic structure, if we define $L = 0$ as the
 293 L position of the X line, then B_n should change sign across $L = 0$. So one might think that
 294 the B_n -dependent terms in (4) would make the greatest contribution to $V_{str,l}$. But B_n is small
 295 (Figure 1e), and the greatest contributions to $V_{str,l}$ come from the B_m and B_l -dependent
 296 terms in (4) (green and blue curves in Figures 3c, respectively).

297 The magnitude of $V_{str,i}$, where $i = L$ or N , can be found from the magnitudes of $V_{str,k}$,
 298 where $k = l, m$, or n , using

$$V_{str,i} = \sqrt{\cos^2(\theta_{i,n}) V_{str,n}^2 + \cos^2(\theta_{i,l}) V_{str,l}^2 + \cos^2(\theta_{i,m}) V_{str,m}^2}, \quad (10)$$

299 where $\cos(\theta_{i,k})$ is the angle between the i (L or N) and k (l, m , or n) directions. Figure 3e
 300 shows $\cos^2 \theta_{i,m}$ for $i = L$ (blue curve) and $i = N$ (red curve). Because these values are
 301 small, especially for $i = N$, the neglect of $V_{str,m}$ in the calculation of $V_{str,N}$ leads to almost
 302 no inaccuracy, and the neglect of $V_{str,m}$ in the calculation of $V_{str,L}$ is not a significant prob-
 303 lem unless $V_{str,m} \gg V_{str,l}$. But Figure 2 shows that $V_{str,m}$ (green dots) does not become much
 304 greater than $V_{str,l}$ unless the minimum eigenvalue λ_{\min} becomes very small ($< 0.1\lambda_0$), for
 305 which $V_{str,m}$ is not expected to be accurate. Therefore, our STD values of $V_{str,N}$ should be
 306 very accurate, and despite the fact that λ_{\min} in Figure 1a (blue curve) is not always above our
 307 desired value for accuracy (dotted black line), there are indications that $V_{str,L}$ may be accu-
 308 rate. These include the fact that neither the maximum or intermediate gradient components
 309 of $V_{str,k}$ increase with decreasing eigenvalue in Figure 2, and the comparison with the veloc-
 310 ity calculated from reconstruction described below.



312 **Figure 4.** Model and observed magnetic field and current density. (a–c) observed (dotted curves) and RQ-
 313 3D model (solid curves) L , M , and N components of \mathbf{B} for the individual MMS spacecraft, using the colors in
 314 the key of panel a; and (d–f) the particle current density \mathbf{J} using the same colors and line styles as for \mathbf{B} . The
 315 gold curves are the average of the observed values (dotted curves) and the model values at the centroid of the
 316 spacecraft positions (solid curves).

3.3 Polynomial reconstruction

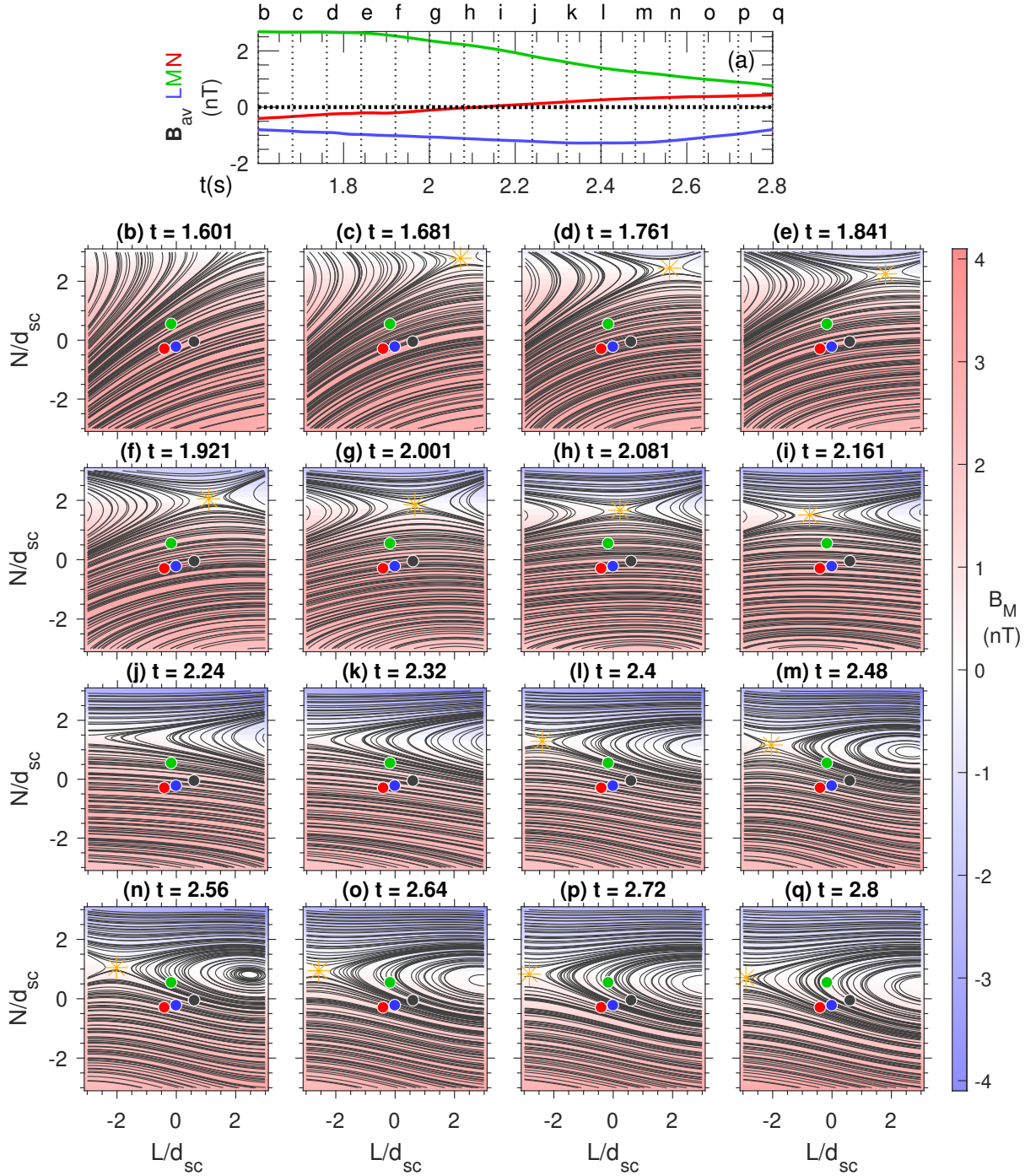
Figure 4 shows that the RQ-3D polynomial model well represents \mathbf{B} and \mathbf{J} during the time interval $t = 1.6$ s to 2.8 s. The J_N component is not as well modeled as the other components, but it is very small compared to the other components of \mathbf{J} . This shows that the model is reasonable in the vicinity of the spacecraft, though it does not necessarily show that the model is accurate away from the spacecraft.

Figure 5 shows reconstruction results for the magnetic field in the L - N plane at $M = 0$, where here L , M , and N are measured with respect to the centroid of the MMS spacecraft, at the origin in Figures 5b–5q. The reconstruction appears to show a reconnection X line (extending normal to the L - N plane, so that it is an X point in that plane), indicated by the gold asterisk, that appears slightly after $t = 1.6$ s. The X line does not move much until about $t = 1.92$ s. Then between $t = 1.92$ s and 2.24 s it moves rapidly in the minus L direction relative to the spacecraft. Later, it reappears near the left (negative L) side of the plot from $t = 2.4$ s to 2.8 s. While the L position of the X line is somewhat variable, the X line appears to move uniformly in the minus N direction relative to the spacecraft.

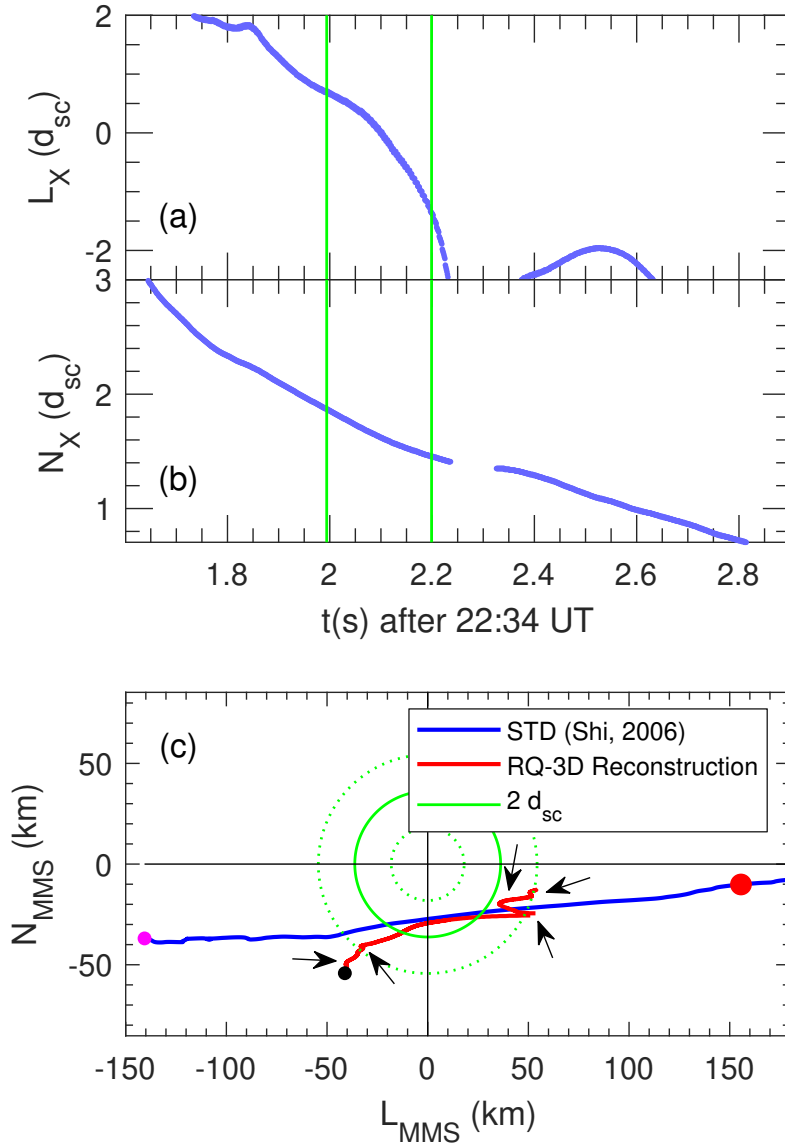
3.4 Path of the spacecraft through the magnetic structure

Figures 6a and 6b show the motion of the reconnection X line relative to the centroid of the MMS spacecraft in the L and N directions, respectively, based on the RQ-3D polynomial reconstruction using data such as in Figure 5. At each time, the position in the L - N plane is found where the in-plane magnetic field is a minimum (indicated by the gold asterisks in Figure 5b–q). (There are also minima corresponding to reconnection O points, but these have been removed from Figure 6.)

The red curve in Figure 6c makes use of the positions from Figures 6a and 6b to show the path of the centroid of the MMS spacecraft relative to the X line, which is at the origin of Figure 6c. The L_{MMS} and N_{MMS} components in Figure 6c have been converted to km using $d_{\text{sc}} = 18.3$ km. The path progresses generally from the left to the right, starting at the black circle. There are some reversals with respect to time of the velocity in the L direction, v_L , at positions indicated by the black arrows. At these positions, all outside a radius of 2 spacecraft spacings ($2 d_{\text{sc}}$) as indicated by the solid green curve, the reconnection X line seems to linger near the periphery of the reconstruction (at a distance of about 2–3 d_{sc}).



322 **Figure 5.** RQ-3D reconstruction of the magnetic field in the L - N plane at $M = 0$. (a) The magnetic field
 323 averaged over the spacecraft, B_{av} ; and (b–q) streamlines of the in-plane magnetic field at $M = 0$ (black curves)
 324 and B_M (color) for B_M directed into the page using the color scale at the right side of the plot. Each plot is
 325 generated at the time indicated in the panel label corresponding to the time of the same label in panel a. The
 326 coordinates L and N are measured relative to the centroid of the MMS spacecraft (at the origin of each panel),
 327 and the positions of the MMS spacecraft are indicated by the colored circles for MMS1 (black circle), MMS2
 328 (red circle), MMS3 (green circle), and MMS4 (blue circle). The gold asterisks are the position of the X line
 329 determined from the in-plane magnetic field minimum.



340 **Figure 6.** Motion of the spacecraft in the L - N plane. (a–b) L and N coordinates of the X line relative to the
 341 centroid of the MMS spacecraft from the RQ-3D reconstruction, (a) L_X and (b) N_X , respectively, in units of
 342 the average spacecraft spacing, d_{sc} , versus time t . (c) Path of the centroid of the MMS spacecraft through the
 343 L - N plane relative to the X line at the origin. The blue curve is from the Spatio-Temporal Difference (STD)
 344 method, and the red curve is from the reconstruction. Both paths start toward the left side of the plot and
 345 progress generally toward the right side. The black circle marks the starting point of the reconstruction path,
 346 and the black arrows represent positions along that path where there is a reversal of the L component of the
 347 velocity, v_L . The magenta circle marks the starting point of the STD path. The solid green circle is at $2d_{sc}$
 348 from the origin.

363 The blue curve shows the path of the MMS spacecraft found from STD. The magenta
 364 circle at the left side of the plot shows the starting point of the path. While the STD path
 365 is shown for the entire time interval of Figures 6a and 6b, 1.6 s to 2.9 s, the points plotted
 366 within the red curve are only for the times when L_X and N_X determined from the recon-
 367 struction are within $\pm 3d_{sc}$, that is, the times for which there are blue data points shown in
 368 Figures 6a and 6b.

369 The STD method yields only velocities, not positions, so the position of the path is de-
 370 termined in the following way. For an X-like reconnection configuration at $(L,N) = (0,0)$,
 371 B_N is expected to change sign with respect to L at $L = 0$, and B_L is expected to change sign
 372 with respect to N at $N = 0$. So the path is adjusted in the left to right direction so that the
 373 N component of the magnetic field averaged over the four spacecraft reverses at $L_{MMS} = 0$
 374 (red curve in Figure 1e at $t = 2.12$ s). This exact procedure cannot be followed to determine
 375 the vertical position of the path using B_L , because $B_{L,av}$ does not reverse during our time in-
 376 terval (green curve in Figure 1e), indicating that the centroid of the spacecraft positions did
 377 not cross the N axis, as depicted in Figure 6c (blue curve). But MMS3 is displaced 10.1 km
 378 in the positive N direction relative to the centroid of the MMS spacecraft. (See the positions
 379 of the green circles in Figure 5b—q relative to the origin at the centroid of the spacecraft.)
 380 And MMS3 did cross the $N = 0$ line, as indicated by a reversal in B_L at 2.81 s (green curve
 381 in Figure 4a just beyond the right side of the plot). At this time the centroid of the MMS po-
 382 sitions was at the large red circle on the right side of the plot. The STD path was adjusted in
 383 the up to down direction by requiring that $N_{MMS} = 0$ was 10.1 km above the red circle.

384 The path of the MMS spacecraft from the reconstruction (red curve) is mostly consis-
 385 tent with that from STD within a distance of $2 d_{sc}$ from the X line (within the solid green
 386 circle). That is, with a slight shift of the blue curve downward, the two curves would almost
 387 exactly lie on top of each other for those parts of the curves that would be within the solid
 388 green circle. During the time that the centroid of the MMS spacecraft is within $2d_{sc}$ of the X
 389 line (2.04 s to 2.16 s, indicated by the vertical solid green lines in Figures 6a and 6b), the L
 390 and N components of the velocity based on the reconstruction were 180 km/s and 32 km/s,
 391 respectively, whereas the L and N components of the velocity based on the STD method
 392 were 236 km/s and 32 km/s, respectively. So the N components of the velocity were the
 393 same for both methods, and the L components agreed within no more than 30% (depending
 394 on how we calculate the percent difference).

395 Note also that both STD and the reconstruction show the largest L component of the
 396 structure velocity at about $t = 2.23$ s (based on the solid blue curve in Figure 3a and the
 397 blue curve in Figure 6a). A more precise comparison is shown in Figure 3a, where the dotted
 398 curves are the L component (cyan dotted curve) and N component (magenta dotted curve)
 399 of the structure velocity based on the motion of the X line in the polynomial reconstruction.
 400 The N components from the reconstruction is quite similar to that from STD (comparing the
 401 red solid and magenta dotted curves in Figure 3a), especially at $t = 2.0$ s and between 2.1 s
 402 and 2.2 s. There are larger differences for the L component (comparing the blue solid and
 403 cyan dotted curves in Figure 3a), but both methods yield increasingly negative velocities with
 404 respect to time, and the average values are similar.

405 **4 Discussion**

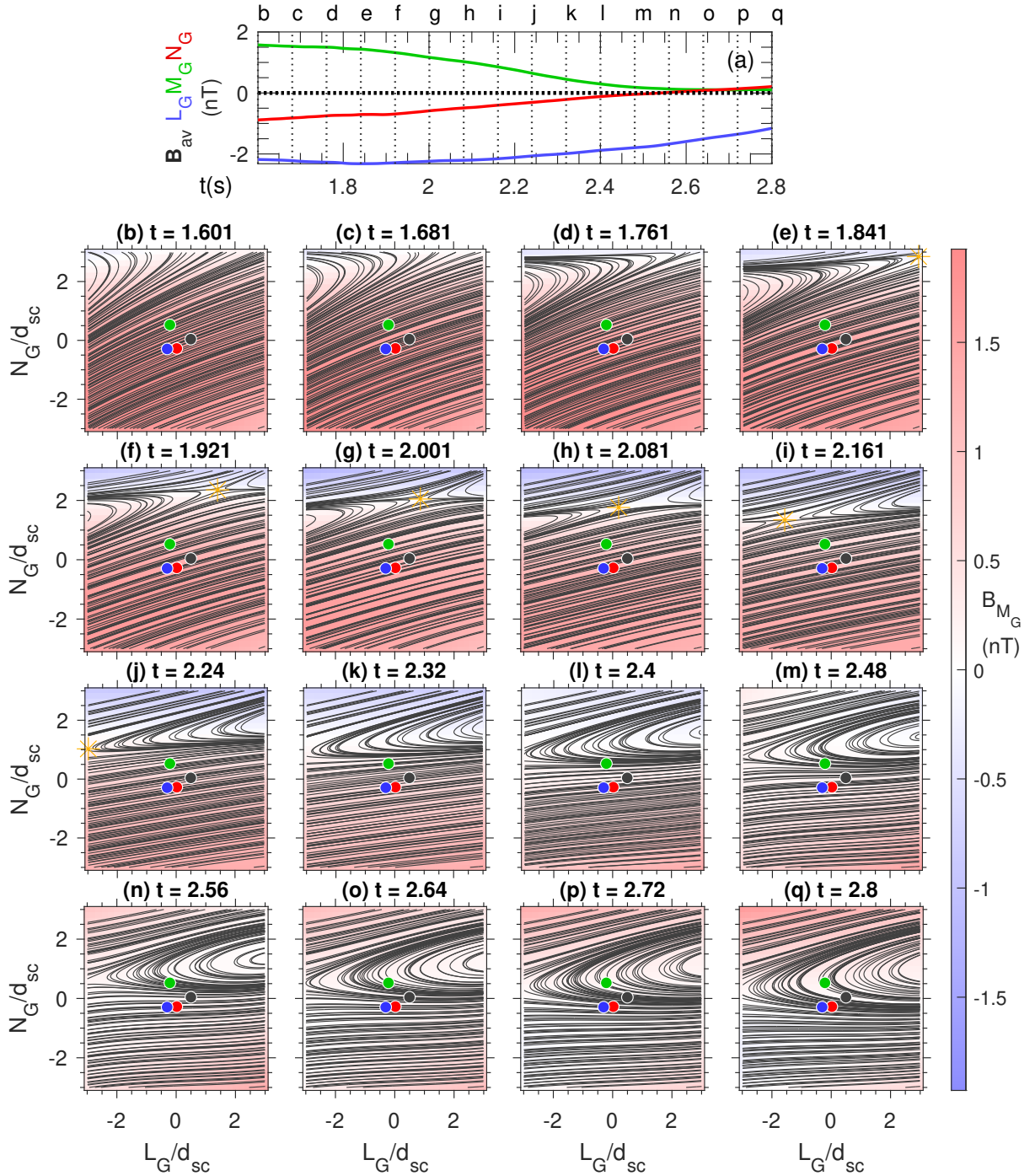
406 We have explained aspects of the Spatio-Temporal Difference (STD) method of *Shi*
 407 *et al.* [2006, 2019], and have shown how STD and the polynomial reconstruction method of
 408 *Denton et al.* [2020] can be used to determine the velocity of the magnetic structure relative
 409 to the MMS spacecraft, and then the path of the MMS spacecraft relative to the X line of
 410 the magnetic structure (Figure 6c). In order to get the path from the STD method, we had to
 411 use the time of reversal in B_N averaged over the MMS spacecraft to align the path in the L
 412 direction, and the time of reversal in B_L as observed by MMS3 to align the path in the N di-
 413 rection. Because the latter event occurred significantly later in time than the closest approach
 414 to the X line (2.814 s; see position of the red circle in Figure 6c), the position of the STD
 415 path probably has more uncertainty in the N direction than in the L direction. So it would
 416 not be unreasonable to shift the path from STD (blue curve in Figure 6c) slightly down to
 417 align it with the path from the reconstruction (red curve in Figure 6c). The two paths would
 418 then agree quite well for the time for which the centroid of the MMS spacecraft is within
 419 $2d_{sc}$ from the X line (within the solid green circle of Figure 6c).

420 The reconstruction is more likely to be accurate when the centroid of the MMS space-
 421 craft is close to the X line, but the path calculated from STD has no such restriction. The
 422 STD and reconstruction paths agree when the centroid of the spacecraft are within a distance
 423 of $2d_{sc}$ from the X line, validating both methods when the MMS spacecraft are close to the X
 424 line. Calculating the velocity of the MMS spacecraft relative to the X line based on these two
 425 methods during the interval of time that the centroid of the spacecraft was within a distance
 426 of $2d_{sc}$ from the X line based on the reconstruction, we found that the N component of the

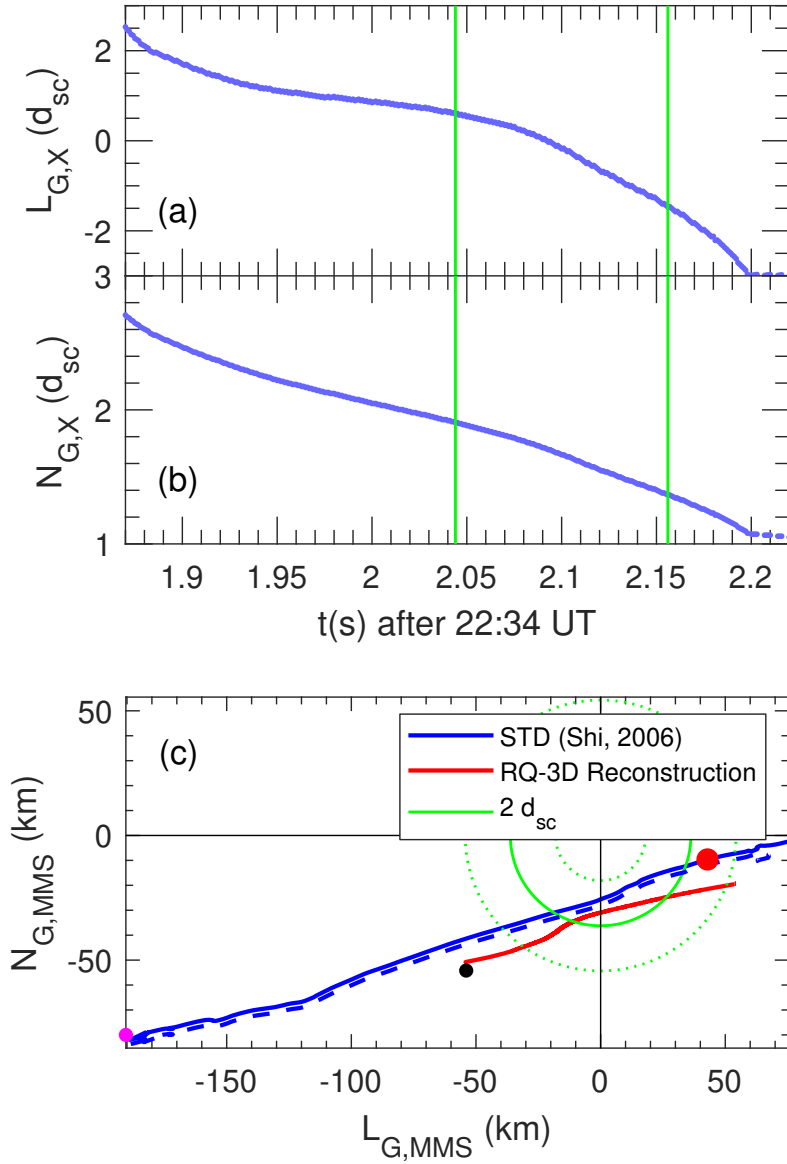
427 velocity from STD and the reconstruction agreed precisely, while the L components agreed
 428 to within no more than 30%. But there is no reason that the STD results should be less accu-
 429 rate when the MMS spacecraft are not close to the X line. So we conclude that the position
 430 of the X line from the reconstruction is only likely to be accurate when the centroid of the
 431 MMS spacecraft is within $2d_{sc}$ from the X line, and the STD velocity is likely to be more ac-
 432 curate than the reconstruction velocity when the MMS spacecraft are farther away from the
 433 X line.

436 As mentioned in section 3.1, *Genestreti et al.* [2018] found L , M , and N directions
 437 (their MDD-B/MVA- v_e coordinate system, coordinate system 14 in their Table A1) that var-
 438 ied by 40° , 39° , and 11° , respectively, from our directions. Their analysis used MDD to get
 439 the N direction, but the maximum variance direction of the electron velocity to get the L
 440 direction. They were strongly motivated by the goal of finding an M direction that yielded
 441 constant E_M . The constancy of E_M follows from Faraday's Law if the reconnection is two-
 442 dimensional (in the L - N plane) and time independent. In other words, this coordinate system
 443 was also motivated by the goal of determining M as the direction of invariance of the mag-
 444 netic field. To avoid confusion with the directions based on MDD, we will indicate these
 445 directions by a "G" subscript. Unfortunately we are not able to accurately calculate the ve-
 446 locity in the L_G - N_G plane using STD, because the velocity in the L_G direction would have
 447 a significant contribution from the velocity in our M direction. Then, because the gradient
 448 in our M direction is very small, the velocity in the L_G direction cannot be reliably deter-
 449 mined. Nevertheless, we project our STD velocity onto the L_G and N_G directions to get what
 450 is probably a lower limit on these velocity components.

454 We also determine the velocity in the L_G - N_G plane using an RQ-3D reconstruction.
 455 Figure 7 shows the reconstructed magnetic field using the same format as Figure 5. In Fig-
 456 ure 7, the X line moves across the field of view from right to left, as in Figure 5, but does
 457 not linger at the periphery of the plot where $L_G/d_{sc} = \pm 3$. Figure 8 is similar to Figure 6,
 458 but showing the motion of the spacecraft with respect to the L_G and N_G coordinates. The
 459 dashed blue curve in Figure 8 shows the path calculated from STD including all velocity
 460 components with eigenvalues to the right of the dotted vertical red line in Figure 2. Thus
 461 a small number of m velocity component values are included in the calculation of the L_G
 462 and N_G components of the STD velocity. The fact that the dashed blue curve in Figure 8 is
 463 slightly closer to the red curve than the blue curve is suggestive that inclusion of the miss-



434 **Figure 7.** RQ-3D reconstruction of the magnetic field in the L_G-N_G plane at $M_G = 0$. Same as Figure 5,
 435 except showing the magnetic field in the L_G-N_G rather than $L-N$ plane.

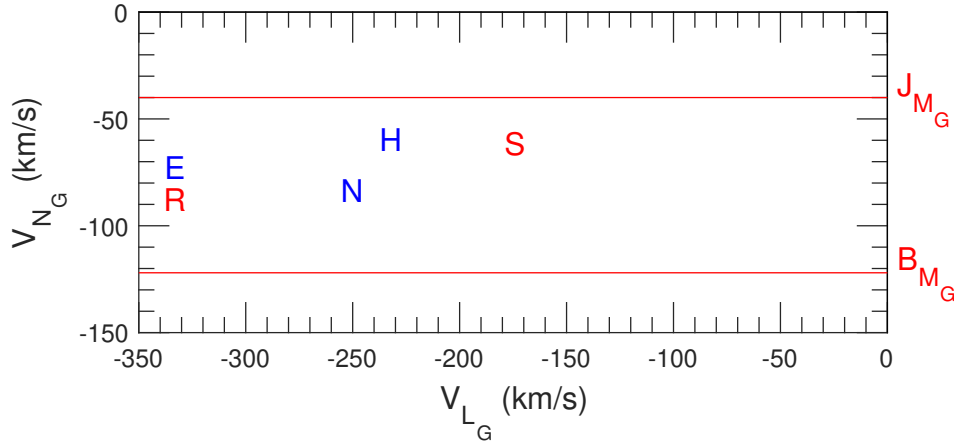


451 **Figure 8.** Motion of the spacecraft in the L_G - N_G plane. Similar to Figure 6, except showing the motion
 452 using the L_G and N_G rather than L and N coordinates. The blue dashed curve in Figure 7c is found from STD
 453 making use of all velocity components to the right of the red vertical dotted line in Figure 2.

466

Table 1. Magnetic structure velocities in the *Genestreti et al.* [2018] L_G - N_G plane

Symbol in Figure 6	θ_L^a ($^\circ$)	V_{L_G} (km/s)	θ_N^b ($^\circ$)	V_{N_G} (km/s)	Reference
B_{M_G}			3.7	-122	This paper, Timing with B_{M_G}
J_{M_G}			11.5	-40	This paper, Timing with J_{M_G}
S	0	-174	0	-61	This paper, STD
R	0	-333	0	-87	This paper, RQ-3D reconstruction
N	0	-250	0	-83	<i>Nakamura et al.</i> [2019]
H	5.0	-232	0.6	-59	<i>Hasegawa et al.</i> [2019]
E	10.6	-333	6.5	-72	<i>Egedal et al.</i> [2019]

^aAngle between the L_G and reference L directions^bAngle between the N_G and reference N directions**Figure 9.** Magnetic structure velocities in the L_G - N_G plane. Velocities calculated in this paper (red sym-

bols) along with velocities in various references (blue symbols), using the symbols listed in Table 1.

ing m component of velocity might possibly lead to better agreement between STD and the polynomial reconstruction.

Figure 9 compares velocity components in the L_G and N_G directions that we calculate to those that have appeared in several other references listed in Table 1. First of all, we use four spacecraft timing analysis using B_{M_G} and J_{M_G} to determine the N_G components of the velocity only [*Dunlop and Woodward, 1998*]. The angle between the timing normal and the *Genestreti et al.* N_G direction, θ_N , is small in both cases, as shown in Table 1. Therefore

474 the timing analysis is approximately giving the velocity in the N direction. But the results
 475 differ greatly depending on the quantity used, as indicated by -122 km/s value found using
 476 B_{M_G} and the -40 km/s value found using J_{M_G} (see the red horizontal lines in Figure 9). The
 477 velocity found from projection of our STD velocity onto the L_G and N_G directions is indi-
 478 cated in Table 1 and Figure 9 by the “S” symbol (red in Figure 9), and for the reconstruction
 479 using the “R” symbol (red in Figure 9). Velocities from *Nakamura et al. [2019]*, *Hasegawa*
 480 *et al. [2019]*, and *Egedal et al. [2019]* are indicated in Table 1 and Figure 9 respectively by
 481 the “N”, “H”, and “E” symbols (blue in Figure 9).

482 The N_G components from STD and RQ-3D and the three papers referenced are fairly
 483 consistent (letter symbols in Figure 9), and lie between the values from the timing analysis
 484 (red horizontal lines in Figure 9). The L_G velocity component from STD is significantly less
 485 in magnitude than the other estimates, probably owing to the problem of evaluating the STD
 486 velocity component in the M_G direction, mentioned previously. The L_G velocity component
 487 from the reconstruction is equal to that from the *Egedal et al. [2019]* reference, and this esti-
 488 mate has the largest magnitude.

489 In the L - N coordinate system based on Minimum Directional Derivative (MDD) anal-
 490 ysis, the STD and reconstruction velocities agree fairly well (within about 30%), at least
 491 when the centroid of the MMS spacecraft is within $2d_{sc}$ of the X line. This would appear
 492 to roughly validate both of these methods (“roughly” because the L components of the ve-
 493 locities in Figure 3a are certainly not exactly the same). Also, the L coordinate in Figure 5
 494 based on MDD seems to be much better aligned with the current sheet than that in Figure 7.

495 There are some differences in results with different averaging of the data. If the data
 496 is smoothed over less than 0.5 s, the reconstruction yields some additional time dependent
 497 behavior. With 0.3 s smoothing, there appears to be coalescence-like merging of a plasmoid
 498 with the large scale island. Because of the shape of the merging plasmoid (elongated in the
 499 L direction), we do not regard this short timescale behavior to be realistic. (It would not be
 500 energetically favorable.) If the data is smoothed over a larger time, some of the intermedi-
 501 ate eigenvalues become even lower than those in Figure 2. But the values of λ_l/λ_0 are still
 502 greater than unity for $t < 2.35$ s. And there is still no increase in the intermediate gradient
 503 (l) velocity component as the eigenvalue decreases such as occurs for the minimum gradient
 504 component (green dots) in Figure 2 for $\lambda_m/\lambda_0 < 0.1$.

505 *Genestreti et al.* [2018], however, argued that relatively small magnetic field calibration
 506 errors could significantly alter the MDD directions. In particular, their Figure 8 suggests that
 507 calibration errors for \mathbf{B} of order 0.05 nT can cause errors in the L and M directions with typ-
 508 ical values of 10° , but ranging from small values to 20° . There is definitely an inconsistency
 509 between the M component directions based on the minimum gradient from MDD or the con-
 510 stancy of E_M , used to validate Genestreti et al.'s coordinate system. This is because the ar-
 511 gument that E_M should be constant is based on supposed invariance of \mathbf{B} in the M direction,
 512 which should be the MDD minimum gradient direction. Genestreti et al. looked for coordi-
 513 nate systems for which the small value E_M was not dependent on the larger E_N . They found
 514 that E_M in the MDD coordinate system varied with E_N , and on average was negative, imply-
 515 ing that reconnection would not be occurring. On the other hand, $E_{M,G}$ was relatively inde-
 516 pendent of $E_{N,G}$. Other results favoring a coordinate system similar to that of Genestreti et
 517 al. are the optimal coordinate system for Electron MHD (EMHD) reconstruction [*Hasegawa*
 518 *et al.*, 2019] and the good correlation between \mathbf{B} and the electron velocity as the magnetic
 519 field rotates from the L to M direction [*Le et al.*, 2010] found in the simulation of this event
 520 by *Egedal et al.* [2019]. This rotation is consistent with the wave reconnection dynamics first
 521 described by *Mandt et al.* [1994], and then later generalized to electron scale structures [*Le*
 522 *et al.*, 2010, 2013].

523 Of course, evaluating the coordinate system based on the constancy of E_M also in-
 524 volves assumptions, two dimensionality, no time dependence, and accurate calculation of
 525 the electric field. But we cannot rule out the possibility that magnetic field calibration er-
 526 rors are affecting the inferred magnetic structure (like the orientation of the current sheet in
 527 Figures 5) and our results for $V_{\text{str},L}$. For that reason, we also calculated the reconstruction
 528 velocity in Genestreti et al.'s coordinate system. The gradient in the N direction, and hence
 529 $V_{\text{str},N}$, however, is much better determined than that in the L direction, and at any rate, the N
 530 directions of both coordinate systems were fairly similar, differing by 11° .

531 Even if the minimum magnetic field gradient direction was determined correctly, re-
 532 sults by *Denton et al.* [2016a, 2018] indicate that the minimum gradient direction can be the
 533 L direction determined to have maximum variation in the magnetic field, which we usually
 534 associate with the reconnection magnetic field. Perhaps some sort of reconciliation for the
 535 difference in the M direction based on the magnetic field gradient or constancy in the electric
 536 field results from the fact that the magnetic field geometry is in some sense approximately
 537 one dimensional based on the relative size of the maximum and intermediate gradient eigen-

538 values in Figure 1a. From that perspective, there are two directions of relatively small spatial
539 inhomogeneity relative to that of the N direction. At any rate, it seems that different kinds of
540 data align themselves better to different coordinate systems.

541 Both STD and the reconstruction would work better if the spacecraft spacing were
542 somewhat larger, so that the gradients would be better determined and λ_k would be larger
543 relative to λ_0 . (The spacing should be not so much larger that the spacecraft are sampling
544 different structures.) Both the STD and reconstruction results strongly depend on the ob-
545 served gradients in the magnetic field components. It is encouraging, however, that the STD
546 L component of the velocity is affected most strongly by the variation of B_M and B_L , and
547 less so (though not insignificantly) by the variation of B_N (Figure 3b), whereas the L com-
548 ponent of the velocity from the polynomial reconstruction is affected mostly by the spatial
549 variation in B_N (since the X line is at the reversal in B_N). Also our estimate for \mathbf{V}_{str} in the
550 *Genestreti et al.* [2018] coordinate system based on the reconstruction did not differ greatly
551 from other velocity estimates (Figure 9).

552 **Acknowledgments**

553 Work at Dartmouth College was supported by NASA grant 80NSSC19K0254. The MMS
554 data set is available on-line at <https://lasp.colorado.edu/mms/sdc/public/links/>.

555 **A: Derivation of STD structure velocity**

556 Expressing (2) as a matrix equation,

$$\mathbf{B}_{dt} = -\mathbf{V}_{\text{str}} \cdot \mathbf{G}, \quad (\text{A.1})$$

557 where \mathbf{B}_{dt} and \mathbf{V}_{str} are row vectors, and

$$\mathbf{G} = \nabla \mathbf{B} \quad (\text{A.2})$$

558 is a matrix with the partial spatial derivatives varying along the column direction.

559 Now we multiply (A.1) by the transpose of G , \mathbf{G}^T , to get

$$\mathbf{B}_{dt} \cdot \mathbf{G}^T = -\mathbf{V}_{\text{str}} \cdot \mathbf{G} \cdot \mathbf{G}^T = -\mathbf{V}_{\text{str}} \cdot \mathbf{M}_G, \quad (\text{A.3})$$

560 where

$$\mathbf{M}_G = \mathbf{G} \cdot \mathbf{G}^T. \quad (\text{A.4})$$

561 Assume that we have used MDD to get the local time dependent gradient directions,
562 n , l and m . At each time, we define a rotation matrix, \mathbf{M} , that has the eigenvectors along the
563 columns.

564 Now we transform to the local eigenvector frame by multiplying (A.3) by \mathbf{M} on the
565 right and using $\mathbf{M} \cdot \mathbf{M}^T = I$, where I is the identity matrix, to get

$$\mathbf{B}_{dt} \cdot \mathbf{M} \cdot \mathbf{M}^T \cdot \mathbf{G}^T \cdot \mathbf{M} = -\mathbf{V}_{\text{str}} \cdot \mathbf{M} \cdot \mathbf{M}^T \cdot \mathbf{M}_G \cdot \mathbf{M}, \quad (\text{A.5})$$

566 or

$$\mathbf{B}_{dt} \cdot \mathbf{G}^T = -\mathbf{V}_{\text{str}} \cdot \mathbf{M}_G. \quad (\text{A.6})$$

567 Then, as described by *Shi et al.* [2006], we can solve for \mathcal{V}_{str} in closed form (equation
568 (3)) using the fact that \mathcal{M}_G is diagonal in the local MDD coordinate system l - m - n with the
569 gradient eigenvalues, λ_k .

570 **B: Model current density**

571 To calculate the current density $\mu_0 \mathbf{J}$ for the Reduced Quadratic model of *Denton et al.*
572 [2020], we simply take the curl of equations (6–8). For instance, $\mu_0 J_l = \partial B_n / \partial m - \partial B_m / \partial n$.

573 The result is:

$$\mu_0 J_l = \frac{\partial B_n}{\partial m} \quad (\text{B.1})$$

$$- \left(\frac{\partial B_m}{\partial n} + \frac{\partial^2 B_m}{\partial n^2} n + \frac{\partial^2 B_m}{\partial n \partial l} l \right)$$

$$\mu_0 J_m = \frac{\partial B_l}{\partial n} + \frac{\partial^2 B_l}{\partial n^2} n \quad (\text{B.2})$$

$$- \left(\frac{\partial B_n}{\partial l} + \frac{\partial^2 B_n}{\partial l^2} l \right)$$

$$\mu_0 J_n = \frac{\partial B_m}{\partial l} + \frac{\partial^2 B_m}{\partial n \partial l} n + \frac{\partial^2 B_m}{\partial l^2} l \quad (\text{B.3})$$

$$- \frac{\partial B_l}{\partial m}$$

574 Note that $\mu_0 \mathbf{J}$ is at most linear with respect to l and n since the curl operation involves a
575 derivative.

576 References

- 577 Alm, L., M. R. Argall, R. B. Torbert, C. J. Farrugia, J. L. Burch, R. E. Ergun, C. T. Russell,
578 R. J. Strangeway, Y. V. Khotyaintsev, P. A. Lindqvist, G. T. Marklund, B. L. Giles, and
579 J. Shuster (2017), EDR signatures observed by MMS in the 16 October event presented in
580 a 2-D parametric space, *J. Geophys. Res.*, *122*(3), 3262–3276, doi:10.1002/2016ja023788.
- 581 Argall, M. R., D. Fischer, O. Le Contel, L. Mirioni, R. B. Torbert, I. Dors, M. Chut-
582 ter, N. J., R. Strangeway, W. Magnes, and C. T. Russell (2018), The Fluxgate-
583 Searchcoil Merged (FSM) Magnetic Field Data Product for MMS, *ArXiv*, doi:
584 <https://arxiv.org/abs/1809.07388>.
- 585 Burch, J. L., T. E. Moore, R. B. Torbert, and B. L. Giles (2015), Magnetospheric Multiscale
586 Overview and Science Objectives, *Space Science Reviews*, doi:10.1007/s11214-015-0164-
587 9.
- 588 Denton, R. E., B. U. O. Sonnerup, H. Hasegawa, T. D. Phan, C. T. Russell, R. J. Strangeway,
589 B. L. Giles, D. Gershman, and R. B. Torbert (2016a), Motion of the MMS spacecraft rel-
590 ative to the magnetic reconnection structure observed on 16 October 2015 at 1307 UT,
591 *Geophys. Res. Lett.*, *43*(11), 5589–5596, doi:10.1002/2016gl069214.
- 592 Denton, R. E., B. U. O. Sonnerup, H. Hasegawa, T. D. Phan, C. T. Russell, R. J. Strange-
593 way, B. L. Giles, and R. B. Torbert (2016b), Reconnection guide field and quadrupolar
594 structure observed by MMS on 16 October 2015 at 1307 UT, *J. Geophys. Res.*, *121*(10),
595 9880–9887, doi:10.1002/2016ja023323.

- 596 Denton, R. E., B. U. O. Sonnerup, C. T. Russell, H. Hasegawa, T. D. Phan, R. J. Strangeway,
597 B. L. Giles, R. E. Ergun, P. A. Lindqvist, R. B. Torbert, J. L. Burch, and S. K.
598 Vines (2018), Determining L-M-N Current Sheet Coordinates at the Magnetopause
599 From Magnetospheric Multiscale Data, *J. Geophys. Res.*, *123*(3), 2274–2295, doi:
600 10.1002/2017ja024619.
- 601 Denton, R. E., R. B. Torbert, H. Hasegawa, I. Dors, K. J. Genestreti, M. R. Argall, D. Gershman,
602 O. Le Contel, J. L. Burch, C. T. Russell, R. J. Strangeway, B. L. Giles, and D. Fischer
603 (2020), Polynomial reconstruction of the reconnection magnetic field observed by multiple
604 spacecraft, *JOURNAL OF GEOPHYSICAL RESEARCH-SPACE PHYSICS*, *125*(2),
605 doi:10.1029/2019JA027481.
- 606 Dunlop, M. W., and T. I. Woodward (1998), Multi-Spacecraft Discontinuity Analysis:
607 Orientation and Motion, in *Analysis Methods for Multi-Spacecraft Data*, edited by
608 G. Paschmann and P. Daly, pp. 271–306, International Space Science Institute, SR-001,
609 Bern Switzerland.
- 610 Egedal, J., J. Ng, A. Le, W. Daughton, B. Wetherton, J. Dorelli, D. Gershman, and
611 A. Rager (2019), Pressure tensor elements breaking the frozen-in law during re-
612 connection in earth's magnetotail, *PHYSICAL REVIEW LETTERS*, *123*(22), doi:
613 {10.1103/PhysRevLett.123.225101}.
- 614 Fischer, D., W. Magnes, C. Hagen, I. Dors, M. W. Chutter, J. Needell, R. B. Torbert,
615 O. Le Contel, R. J. Strangeway, G. Kubin, A. Valavanoglou, F. Plaschke, R. Nakamura,
616 L. Mirioni, C. T. Russell, H. K. Leinweber, K. R. Bromund, G. Le, L. Kepko, B. J. Anderson,
617 J. A. Slavin, and W. Baumjohann (2016), Optimized merging of search coil and
618 fluxgate data for MMS, *Geoscientific Instrumentation Methods and Data Systems*, *5*(2),
619 521–530, doi:10.5194/gi-5-521-2016.
- 620 Genestreti, K. J., T. K. M. Nakamura, R. Nakamura, R. E. Denton, R. B. Torbert, J. L. Burch,
621 F. Plaschke, S. A. Fuselier, R. E. Ergun, B. L. Giles, and C. T. Russell (2018), How accurately
622 can we measure the reconnection rate E_M for the MMS diffusion region event of
623 2017-07-11?, *J. Geophys. Res.*, *123*.
- 624 Hasegawa, H., R. E. Denton, R. Nakamura, K. J. Genestreti, T. K. M. Nakamura, K. J.
625 Hwang, T. D. Phan, R. B. Torbert, L. Burch, B. L. Giles, D. J. Gershman, C. T. Russell,
626 R. J. Strangeway, P. A. Lindqvist, Y. V. Khotyaintsev, R. E. Ergun, N. Kitamura, and
627 Y. Saito (2019), Reconstruction of the Electron Diffusion Region of Magnetotail Reconnection
628 seen by the MMS Spacecraft on 11 July 2017, *J. Geophys. Res.*, *124*(1), 122–138,

- 629 doi:10.1029/2018ja026051.
- 630 Hesse, M., T. Neukirch, K. Schindler, M. Kuznetsova, and S. Zenitani (2011), The Diffusion
631 Region in Collisionless Magnetic Reconnection, *Space Science Reviews*, *160*(1-4), 3–23,
632 doi:10.1007/s11214-010-9740-1.
- 633 Hesse, M., N. Aunai, J. Birn, P. Cassak, R. E. Denton, J. F. Drake, T. Gombosi, M. Hoshino,
634 W. Matthaeus, D. Sibeck, and S. Zenitani (2014), Theory and Modeling for the Magneto-
635 spheric Multiscale Mission, *Space Science Reviews*, doi:10.1007/s11214-014-0078-y.
- 636 Le, A., J. Egedal, W. Fox, N. Katz, A. Vrublevskis, W. Daughton, and J. F. Drake (2010),
637 Equations of state in collisionless magnetic reconnection, *Phys. Plasmas*, *17*(5), doi:
638 10.1063/1.3309425.
- 639 Le, A., J. Egedal, O. Ohia, W. Daughton, H. Karimabadi, and V. S. Lukin (2013), Regimes
640 of the Electron Diffusion Region in Magnetic Reconnection, *Phys. Rev. Lett.*, *110*(13), doi:
641 10.1103/PhysRevLett.110.135004.
- 642 Le Contel, O., P. Leroy, A. Roux, C. Coillot, D. Alison, A. Bouabdellah, L. Mirioni, L. Mes-
643 lier, A. Galic, M. C. Vassal, R. B. Torbert, J. Needell, D. Rau, I. Dors, R. E. Ergun,
644 J. Westfall, D. Summers, J. Wallace, W. Magnes, A. Valavanoglou, G. Olsson, M. Chut-
645 ter, J. Macri, S. Myers, S. Turco, J. Nolin, D. Bodet, K. Rowe, M. Tanguy, and B. de la
646 Porte (2016), The Search-Coil Magnetometer for MMS, *Space Science Reviews*, *199*(1-4),
647 257–282, doi:10.1007/s11214-014-0096-9.
- 648 Mandt, M. E., R. E. Denton, and J. F. Drake (1994), TRANSITION TO WHISTLER ME-
649 DIATED MAGNETIC RECONNECTION, *Geophys. Res. Lett.*, *21*(1), 73–76, doi:
650 10.1029/93gl03382.
- 651 Manuzzo, R., G. Belmont, L. Rezeau, F. Califano, and R. E. Denton (2019), Crossing of
652 Plasma Structures by Spacecraft: A Path Calculator, *JOURNAL OF GEOPHYSICAL*
653 *RESEARCH-SPACE PHYSICS*, *124*(12), 10,119–10,140, doi:10.1029/2019JA026632.
- 654 Nakamura, R., K. J. Genestreti, T. Naltamura, W. Baumjohann, A. Varsani, T. Nagai,
655 N. Bessho, J. L. Burch, R. E. Denton, J. P. Eastwood, R. E. Ergun, D. J. Gershman, A. L.
656 Giles, I. Hasegaw, M. Hesse, P.-A. Lindqvist, H. T. Russell, U. E. Stawarz, R. J. Strange-
657 way, and R. B. Torber (2019), Structure of the Current Sheet in the 11 July 2017 Electron
658 Diffusion Region Event, *Journal of Geophysical Research-Space Physics*, *124*(2), 1173–
659 1186, doi:10.1029/2018JA026028.
- 660 Pollock, C., T. Moore, A. Jacques, J. Burch, U. Gliese, Y. Saito, T. Omoto, L. Avanov,
661 A. Barrie, V. Coffey, J. Dorelli, D. Gershman, B. Giles, T. Rosnack, C. Salo, S. Yokota,

- 662 M. Adrian, C. Aoustin, C. Auletta, S. Aung, V. Bigio, N. Cao, M. Chandler, D. Chor-
 663 nay, K. Christian, G. Clark, G. Collinson, T. Corris, A. D. L. Santos, R. Devlin, T. Diaz,
 664 T. Dickerson, C. Dickson, A. Diekmann, F. Diggs, C. Duncan, A. Figueroa-Vinas, C. Fir-
 665 man, M. Freeman, N. Galassi, K. Garcia, G. Goodhart, D. Guererro, J. Hageman, J. Han-
 666 ley, E. Hemminger, M. Holland, M. Hutchins, T. James, W. Jones, S. Kreisler, J. Kujawski,
 667 V. Lavu, J. Lobell, E. LeCompte, A. Lukemire, E. MacDonald, A. Mariano, T. Mukai,
 668 K. Narayanan, Q. Nguyen, M. Onizuka, W. Paterson, S. Persyn, B. Piepgrass, F. Cheney,
 669 A. Rager, T. Raghuram, A. Ramil, L. Reichenthal, H. Rodriguez, J. Rouzaud, A. Rucker,
 670 Y. Saito, M. Samara, J.-A. Sauvaud, D. Schuster, M. Shappirio, K. Shelton, D. Sher,
 671 D. Smith, K. Smith, S. Smith, D. Steinfeld, R. Szymkiewicz, K. Tanimoto, J. Taylor,
 672 C. Tucker, K. Tull, A. Uhl, J. Vloet, P. Walpole, S. Weidner, D. White, G. Winkert, P.-
 673 S. Yeh, and M. Zeuch (2016), Fast Plasma Investigation for Magnetospheric Multiscale,
 674 *Space Science Reviews*, doi:10.1007/s11214-016-0245-4.
- 675 Robert, P., M. W. Dunlop, A. Roux, and G. Chanteur (1998), Accuracy of current density de-
 676 termination, in *Analysis Methods for Multi-Spacecraft Data*, edited by G. Paschmann and
 677 P. Daly, pp. 395–418, International Space Science Institute, SR-001, Bern Switzerland.
- 678 Russell, C. T., B. J. Anderson, W. Baumjohann, K. R. Bromund, D. Dearborn, D. Fischer,
 679 G. Le, H. K. Leinweber, D. Leneman, W. Magnes, J. D. Means, M. B. Moldwin, R. Naka-
 680 mura, D. Pierce, F. Plaschke, K. M. Rowe, J. A. Slavin, R. J. Strangeway, R. Torbert,
 681 C. Hagen, I. Jernej, A. Valavanoglou, and I. Richter (2016), The Magnetospheric Multi-
 682 scale Magnetometers, *Space Science Reviews*, doi:10.1007/s11214-014-0057-3.
- 683 Shi, Q. Q., Z. Y. Pu, H. Zhang, S. Y. Fu, C. J. Xiao, Q. G. Zong, T. A. Fritz, and Z. X. Liu
 684 (2005), Simulation studies of high-latitude magnetospheric boundary dynamics, *Surveys*
 685 *in Geophysics*, 26(1-3), 369–386, doi:10.1007/s10712-005-1900-6.
- 686 Shi, Q. Q., C. Shen, M. W. Dunlop, Z. Y. Pu, Q. G. Zong, Z. X. Liu, E. Lucek, and
 687 A. Balogh (2006), Motion of observed structures calculated from multi-point mag-
 688 netic field measurements: Application to Cluster, *Geophys. Res. Lett.*, 33(8), doi:
 689 10.1029/2005gl025073.
- 690 Shi, Q. Q., A. M. Tian, S. C. Bai, H. Hasegawa, A. W. Degeling, Z. Y. Pu, M. Dunlop, R. L.
 691 Guo, S. T. Yao, Q. G. Zong, Y. Wei, X. Z. Zhou, S. Y. Fu, and Z. Q. Liu (2019), Dimen-
 692 sionality, Coordinate System and Reference Frame for Analysis of In-Situ Space Plasma
 693 and Field Data, *Space Science Reviews*, 215(4), doi:10.1007/s11214-019-0601-2.

- 694 Sonnerup, B. O. U. (1979), Magnetic field reconnection, in *Solar System Plasma Physics*,
695 vol. 3 (A79-53667 24-46), pp. 45–108, North-Holland Publishing Co., Amsterdam.
- 696 Sonnerup, B. U., and L. J. Cahill (1967), Magnetopause Structure and Attitude from Ex-
697 plorer 12 Observations, *Journal of Geophysical Research*, 72(1).
- 698 Sonnerup, B. U. O., and M. Scheible (1998), Minimum and maximum variance analysis,
699 in *Analysis Methods for Multi-Spacecraft Data*, edited by G. Paschmann and P. Daly, pp.
700 185–220, International Space Science Institute, SR-001, Bern Switzerland.
- 701 Torbert, R. B., J. L. Burch, T. D. Phan, M. Hesse, M. R. Argall, J. Shuster, R. E. Ergun,
702 L. Alm, R. Nakamura, K. J. Genestreti, D. J. Gershman, W. R. Paterson, D. L. Turner,
703 I. Cohen, B. L. Giles, C. J. Pollock, S. Wang, L.-J. Chen, J. E. Stawarz, J. P. Eastwood,
704 K. J. Hwang, C. Farrugia, I. Dors, H. Vaith, C. Mouikis, A. Ardakani, B. H. Mauk, S. A.
705 Fuselier, C. T. Russell, R. J. Strangeway, T. E. Moore, J. F. Drake, M. A. Shay, Y. V.
706 Khotyaintsev, P.-A. Lindqvist, W. Baumjohann, F. D. Wilder, N. Ahmadi, J. C. Dorelli,
707 L. A. Avanov, M. Oka, D. N. Baker, J. F. Fennell, J. B. Blake, A. N. Jaynes, O. Le Contel,
708 S. M. Petrinen, B. Lavraud, and Y. Saito (2018a), Electron-scale dynamics of the diffusion
709 region during symmetric magnetic reconnection in space, *Science*, 362(6421), 1391–+,
710 doi:10.1126/science.aat2998.
- 711 Torbert, R. B., J. L. Burch, M. R. Argall, C. J. Farrugia, I. Dors, D. Payne, K. J. Genestreti,
712 A. J. Rogers, R. J. Strangeway, T. Phan, R. Ergun, Y. V. Khotyaintsev, and B. L. Giles
713 (2018b), Energetics within Selected MMS Encounters of Electron Diffusion Regions,
714 AGU, Abstract SM33A-02 presented at the 2018 Fall Meeting, Washington DC, 10-14
715 Dec.
- 716 Torbert, R. B., I. Dors, M. R. Argall, K. J. Genestreti, J. L. Burch, C. J. Farrugia, T. G.
717 Forbes, B. L. Giles, and R. J. Strangeway (2020), A New Method of 3-D Magnetic
718 Field Reconstruction, *Geophysical Research Letters*, 47(3), e2019GL085,542, doi:
719 10.1029/2019GL085542.
- 720 Vasyliunas, V. (1975), Theoretical models of magnetic-field line merging .1., *Reviews Of*
721 *Geophysics*, 13(1), 303–336, doi:10.1029/RG013i001p00303.
- 722 Yao, S. T., Q. Q. Shi, Z. Y. Li, X. G. Wang, A. M. Tian, W. J. Sun, M. Hamrin, M. M. Wang,
723 T. Pitkanen, S. C. Bai, X. C. Shen, X. F. Ji, D. Pokhotelov, Z. H. Yao, T. Xiao, Z. Y. Pu,
724 S. Y. Fu, Q. G. Zong, A. De Spiegeleer, W. Liu, H. Zhang, and H. Reme (2016), Propaga-
725 tion of small size magnetic holes in the magnetospheric plasma sheet, *J. Geophys. Res.*,
726 121(6), 5510–5519, doi:10.1002/2016ja022741.

727 Yao, S. T., Q. Q. Shi, R. L. Guo, Z. H. Yao, A. M. Tian, A. W. Degeling, W. J. Sun, J. Liu,
728 X. G. Wang, Q. G. Zong, H. Zhang, Z. Y. Pu, L. H. Wang, S. Y. Fu, C. J. Xiao, C. T. Rus-
729 sell, B. L. Giles, Y. Y. Feng, T. Xiao, S. C. Bai, X. C. Shen, L. L. Zhao, and H. Liu (2018),
730 Magnetospheric Multiscale Observations of Electron Scale Magnetic Peak, *Geophys. Res.*
731 *Lett.*, *45*(2), 527–537, doi:10.1002/2017gl075711.